frontiers in Physics

ORIGINAL RESEARCH
published: 07 June 2017
doi: 10.3389/fphy.2017.00017

Analysis of an Integrated 8-Channel Tx/Rx Body Array for Use as a Body Coil in 7-Tesla MRI

Stephan Orzada[1], Andreas K. Bitz[2,3], Sören Johst[1], Marcel Gratz[1,4], Maximilian N. Völker[1], Oliver Kraff[1], Ashraf Abuelhaija[5], Thomas M. Fiedler[2], Klaus Solbach[5], Harald H. Quick[1,4] and Mark E. Ladd[1,2,6]*

[1] Erwin L. Hahn Institute for Magnetic Resonance Imaging, University of Duisburg-Essen, Essen, Germany, [2] Medical Physics in Radiology, German Cancer Research Center, Heidelberg, Germany, [3] Electromagnetic Theory and Applied Mathematics, Faculty of Electrical Engineering and Information Technology, FH Aachen—University of Applied Sciences, Aachen, Germany, [4] High-Field and Hybrid MR Imaging, Essen University Hospital, Essen, Germany, [5] RF & Microwave Technology, University of Duisburg-Essen, Duisburg, Germany, [6] Faculty of Physics and Astronomy and Faculty of Medicine, University of Heidelberg, Heidelberg, Germany

OPEN ACCESS

Edited by:
He (Henry) Zhu,
Vanderbilt University, United States

Reviewed by:
Nicolas Francisco Lori,
LANEN, INCYT, INECO Foundation, Argentina
Alexander Raaijmakers,
University Medical Center Utrecht, Netherlands
Ryan Brown,
New York University School of Medicine, United States

***Correspondence:**
Stephan Orzada
stephan.orzada@uni-due.de

Specialty section:
This article was submitted to Interdisciplinary Physics, a section of the journal Frontiers in Physics

Received: 06 February 2017
Accepted: 23 May 2017
Published: 07 June 2017

Citation:
Orzada S, Bitz AK, Johst S, Gratz M, Völker MN, Kraff O, Abuelhaija A, Fiedler TM, Solbach K, Quick HH and Ladd ME (2017) Analysis of an Integrated 8-Channel Tx/Rx Body Array for Use as a Body Coil in 7-Tesla MRI. Front. Phys. 5:17. doi: 10.3389/fphy.2017.00017

Object: In this work an 8-channel array integrated into the gap between the gradient coil and bore liner of a 7-Tesla whole-body magnet is presented that would allow a workflow closer to that of systems at lower magnetic fields that have a built-in body coil; this integrated coil is compared to a local 8-channel array built from identical elements placed directly on the patient.

Materials and Methods: SAR efficiency and the homogeneity of the right-rotating B1 field component (B_1^+) are investigated numerically and compared to the local array. Power efficiency measurements are performed in the MRI System. First *in vivo* gradient echo images are acquired with the integrated array.

Results: While the remote array shows a slightly better performance in terms of (B_1^+) homogeneity, the power efficiency and the SAR efficiency are inferior to those of the local array: the transmit voltage has to be increased by a factor of 3.15 to achieve equal flip angles in a central axial slice. The g-factor calculations show a better parallel imaging g-factor for the local array. The field of view of the integrated array is larger than that of the local array. First *in vivo* images with the integrated array look subjectively promising.

Conclusion: Although some RF performance parameters of the integrated array are inferior to a tight-fitting local array, these disadvantages might be compensated by the use of amplifiers with higher power and the use of local receive arrays. In addition, the distant placement provides the potential to include more elements in the array design.

Keywords: 7 Tesla, integrated body array, whole body, MRI, body coil

INTRODUCTION

Since the early days of MRI, a steady drive to higher field strength can be noted. While a higher field strength results in an increase in obtainable SNR, the shorter wavelength of the electromagnetic fields at the higher resonance frequencies can lead to severe problems [1, 2]. At 7 T one of the main imaging challenges are inhomogeneous transmit fields (B_1^+) that can lead to complete signal voids in the field of view, especially in the torso where the body dimensions are large [3]. Not only

do these inhomogeneities affect the SNR, but also lead to varying contrast throughout the field of view, reducing the clinical utility of the resulting images.

Nevertheless, an increasing number of clinical feasibility studies at 7 T aim at regions where imaging is hampered by these severe transmit inhomogeneities, for example liver [4, 5], kidneys [6], prostate [7, 8], female pelvis [9], the hip joints [10, 11], the heart [12], the spinal cord [13], and the breasts [14, 15], or they cover extended regions such as the complete lower extremities [16].

To cope with the severe inhomogeneities, several techniques have been proposed in the literature. Examples of these techniques are RF shimming [17, 18], 3D tailored radiofrequency pulses [19], Transmit SENSE [20, 21], and TIAMO [22]. While these methods may approach the problem differently, most share the need for multichannel transmit arrays.

Most of the multichannel arrays that have been proposed for imaging the torso and/or large proportions of the body at 7 T are local transmit/receive (Tx/Rx) arrays that consist of various types of individual elements such as microstrip lines [18, 23–25], microstrip lines with meanders [26], loops [13, 27–29], or dipole antennas [30–33]. Some of these coils can be quite bulky and have thicknesses of more than 5 cm [26, 30, 31]. This reduces the usable diameter within the bore and can lead to an exclusion of larger patients.

Already at 3 T there is a certain need for control of the transmit field to reduce inhomogeneity. Therefore, body coils with two [34] or more channels [35] were introduced to enhance image quality and SAR performance. These approaches allow the usual clinical workflow and the use of standard receive arrays, while at the same time increasing the degrees of freedom for transmit field manipulation. The lower impact of the inhomogeneities at 3 T have thus far not made transmit arrays with more than two channels, and therefore the additional investment, a necessity for clinical systems. Even at 4 T it is possible to perform high-quality imaging using a volume resonator with a clever design as shown by Vaughan et al. [36]. At 7 T, however, a multi-channel body array has the potential to introduce a much larger gain.

Since 7 T systems have no vendor-integrated body coil, the space between the inner cladding of the magnet (bore liner) and the gradient coil can potentially be used for the integration of a Tx or Tx/Rx body array, leaving more space inside the bore and allowing easier utilization of dedicated receive arrays [3, 37], potentially improving SNR and parallel imaging performance and allowing a workflow closer to clinical standard. Since current 7 T body systems have a usable diameter of 60 cm, while more and more clinical systems have 70 cm, freeing space in the bore to accommodate larger patients is important.

Important points to be considered when designing a transmit body coil are the power demands and the impact on local SAR. Body coils with a larger inner volume have higher power demand and the power demand is further increased with increasing field strength [36]. Local SAR can be reduced in some cases by reducing the conservative E-fields at the surface by increasing the distance between the elements and the tissue [38].

In this paper we present an integrated 8-channel Tx/Rx body array for MRI at 7 T. We compare the performance of this array to a local 8-channel Tx/Rx array with the same type of elements.

MATERIALS AND METHODS

MR System

The integrated body coil was designed for a Siemens Magnetom 7 T system (Siemens Healthcare, Erlangen, Germany) equipped with an AS095 gradient coil. If the sound and vibration-dampening material is disregarded, the space between the 10-mm-thick fiberglass bore liner and the gradient coil is 34 mm in this system.

A custom 8-channel RF shimming system [39] was used to drive both eight-channel coils. Each channel has a peak power of 1 kW, of which 790 W are delivered to the coil plug after accounting for cable losses.

8-Channel Local Coil

The 8-channel local coil is shown in **Figure 1a**. It is identical to one already described in the literature [26]. The array consists of 8 elements, 4 of which are placed in a PMMA (polymethyl methacrylate, acrylic glass) box in the patient table, while the 4 anterior elements are placed in individual boxes made of polycarbonate interconnected with neoprene to form a flexible arrangement. The minimum distance between the elements and the body is 3 cm, independent of body size. The elements are connected to T/R switches with pre-amplifiers (Stark Contrast, Erlangen, Germany) in a multi-purpose box located at the head of the patient table by low-loss cables (Aircell 5, SSB Electronic GmbH, Lippstadt, Germany) with an appropriate length to ensure pre-amp decoupling.

The transmit elements are micro strip lines with meanders which are used due to their intrinsic decoupling and high penetration depth as described in the literature [40]. The distance between ground plane and micro strip is 20 mm, and the width of the ground plane is 100 mm. The length of the meanders in the terminology of Rietsch et al. [40] is 32.5 mm. The end capacitors are non-magnetic 1 pF capacitors with a maximum DC working voltage of 2,500 V (Voltronics 25 Series, Voltronics Corporation, Salisbury, USA). The 180° line of the balun for the central feeding network is fabricated from semi-rigid cable (EZ_141_CU_TP, Huber+Suhner AG, Herisau, Swiss).

8-Channel Remote Coil

Figure 1b shows the 8-channel coil array placed on the bore liner. The outer diameter of the bore liner is 61.5 cm and the wall thickness is 1 cm. The array consists of a circular arrangement of 8 microstrip line elements with meanders, which are identical to the ones used in the local array and were not optimized for the remote array. These elements were chosen due to their low coupling even when not heavily loaded [40]. The distance between the microstrip and the surface of the bore liner is 5 mm minimum. Due to the dielectric loading of the meanders introduced by the proximity of the bore liner, the length of the meanders was shortened to 30 mm. Each single element is 25 cm long and 9 cm wide. The distance between the ground plane and conducting structure on the microstrip PCB is 20 mm.

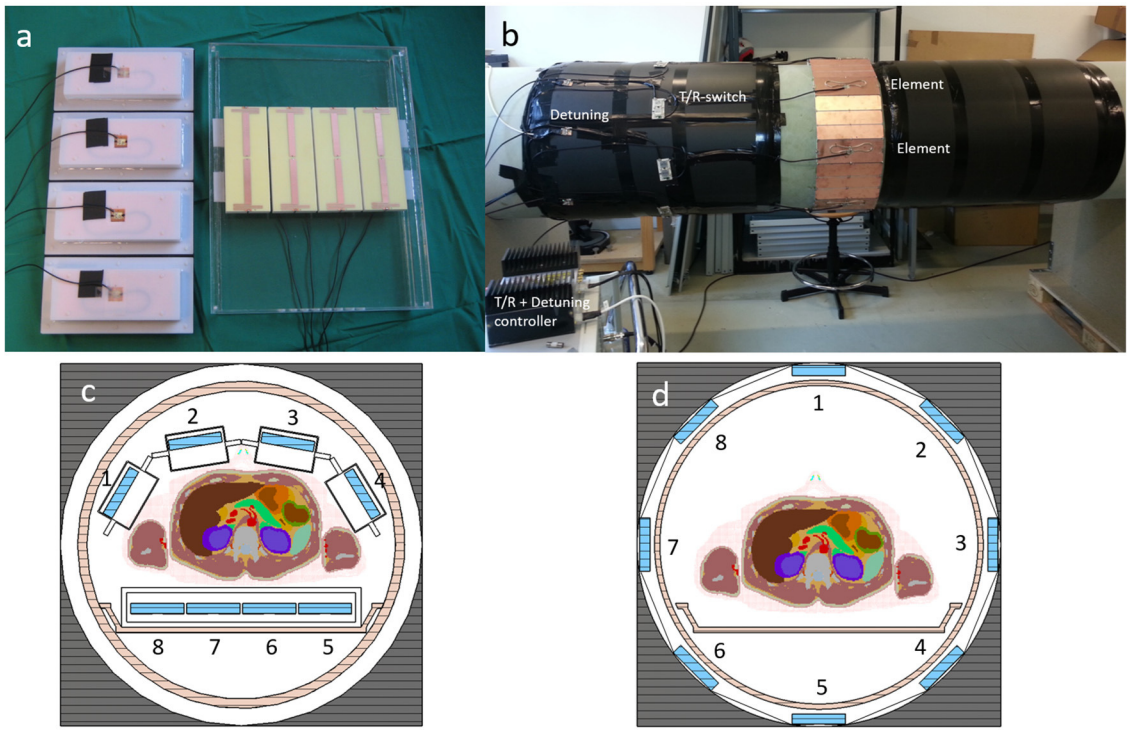

FIGURE 1 | The two coil setups under comparison. **(a)** The local coil, consisting of flexible anterior half and rigid posterior half, **(b)** the 8-channel integrated body array including T/R switches, detuning boards, and PIN diode controller. The black material is sound-dampening foam. Panels **(c,d)** show CAD models of the two coils. The positions of the numbered elements are highlighted in blue.

The ground planes of the individual elements are interconnected with slotted PCBs to create a continuous circumferential ground plane; the slots are intended to prevent eddy currents and are bridged by 1,000 pF non-magnetic capacitors (Voltronics 11 Series, Voltronics Corporation, Salisbury, USA).

The 180° line of the balun for the central feeding network is fabricated from semi-rigid cable (EZ_141_CU_TP, Huber+Suhner AG, Herisau, Switzerland). The end capacitors of the elements are non-magnetic 1 pF (Voltronics 25 Series), whereas the matching network consists of capacitors from the Voltronics 11 Series with 1,000 V working voltage.

The elements are connected to custom-built, compact T/R switches with a design similar to Watkins et al. [41]; the only difference to the published design is that all components were placed on one side of a 81 by 42 mm PCB rather than using a folded layout. An appropriate length of low-loss cable (Aircell 5, SSB-Electronic GmbH, Lippstadt, Germany) to transform the impedance of the pre-amp ensures pre-amp decoupling of at least 12 dB; the decoupling was measured with a double pick-up coil. Detuning of the elements is performed with dedicated detuning boards containing PIN diodes that produce an RF short circuit of the transmit cable to ground when a forward current is applied. These detuning boards are placed in the transmit chain between the radio frequency power amplifiers (RFPAs) and the T/R switches (**Figure 1**) with an appropriate length of cable to transform the short circuit to an impedance that detunes the elements. In addition to allowing detuning of the elements, this placement reduces spurious noise from the RFPAs during reception. The detuning boards contain two antiparallel PIN diodes (MA4P7446F-1091T, MACOM Technology Solutions, Lowell, MA, USA) that are placed in series with one another. In this configuration they can handle powers in the low kW range with only 12 V reverse bias. A non-magnetic capacitor (Voltronics 11 Series) with 47 pF is placed in series with the PIN diodes to cancel out the parasitic inductances of the diodes in forward mode.

The reverse voltage and forward current for the PIN diodes are supplied by a 2-channel controller. This controller is placed directly at the back of the magnet. In forward mode it delivers 1.2 A as a current source, whereas in reverse mode it delivers 12 V as a voltage source. Switching between the two states takes 5 µs. The correct timing and logic for switching are supplied via optical connections from a custom-built control unit in the equipment room of the scanner.

The tuning and matching of the array was done outside of the magnet, loaded with a male volunteer (1.87 m, 82 kg). The patient table had to be substituted with a wooden board, mimicking the position that the volunteer would assume in the magnet. Tuning and matching are both fixed and cannot be changed after integration of the coil, since the elements are inaccessible.

The bore liner is clad with vibration dampening material (Ear-Foam, Aearo Technologies LLC, Indianapolis, USA) to reduce acoustic noise. A small section was removed to accommodate the array, as can be seen in **Figure 1**.

Numerical Simulations

All simulations were performed using the finite integration technique (FIT) in CST Studio Suite (CST AG, Darmstadt, Germany). Both coils were simulated including housing, bore liner, magnet bore, and patient table; the gradient coil was considered as a block of perfect electrically conductive material to account for the reduced diameter vs. the warm bore in the center of the magnet. A male body model (1.74 m, 70 kg, "Duke" 42) with a tissue resolution of 2 mm^3 was placed inside both coils in a position suitable for abdominal MRI. The simulation model was discretized by use of a graded mesh with about 66 million mesh cells and a minimum mesh step of 0.5 mm. The maximum allowed mesh edge of the graded mesh was set to lambda/30 at the highest frequency of interest (350 MHz). The minimum mesh edge in regions with small geometrical details (e.g., feed point of meander elements, lumped elements, or meander structures) was set to 0.5 mm. Further, a mesh refinement at metallic edges with 2 additional cells around the edge was selected.

From the simulation results, virtual observation point (VOP) [43] SAR matrices were calculated. Averaging of the local specific absorption rate for any 10 g tissue mass was performed according to IEEE/IEC 62704-1. Since the exact locations of the averaging volumes could not be extracted from the CST data, it was not possible to know whether an averaging volume contains arms only before performing the VOP calculation. Therefore, different SAR limits for the extremities could not be taken into account. With these VOPs and the B_1^+ results from the simulations, 50,000 random shims (amplitude range 0–1 W and phase range 0°–360°) and a magnitude least square (MLS) shim were calculated for a central axial slice with a thickness of 3.8 mm in the abdomen for each coil. Furthermore, the voxel-wise SAR efficiency was calculated: for each voxel ($3.8 \times 3.8 \times 3.8\,mm^3$) in both a coronal and an axial slice, a shim was calculated that maximized $\left|B_1^+\right| / \sqrt{SAR_{10g}}$. Optimization was performed with a Nelder-Mead simplex search algorithm [44]. Since this algorithm can run into local optima, the best result of 12 random starting points was used. Here SAR_{10g} is the maximum local SAR anywhere within the body. This measure provides the maximum obtainable B_1^+ at any point for a given SAR_{10g}. The relative standard deviation in B_1^+ was used as a measure of homogeneity.

S-Parameter Measurements

S-parameters for the integrated coil array were measured with the coil placed in the magnet bore, loaded with the same male volunteer (1.87 m, 82 kg) used to tune and match the coil before integration. S-parameters for the local array were measured with the same volunteer.

MR Experiments

A routinely applied quality assurance (QA) protocol was used to investigate the influence of the integrated body coil on a local Tx/Rx coil when the integrated coil was permanently detuned. The local coil was a 1-ch Tx/32-ch Rx head coil (Nova Medical, Inc., Wilmington, USA) loaded with a tissue simulating phantom ($\varepsilon' = 55$, $\sigma = 0.6$ S/m). The QA protocol includes tests to check for the performance of the local RF coil as well as gradient and system stability. The proper function of the RF coil was verified by B1, SNR, and coupling measurements (i.e., noise correlation). Unwanted noise sources and RF spikes were searched for with noise measurements. System stability was measured with high-duty-cycle EPI bold imaging (TR 1,000 ms, TE 30 ms, Echo Spacing 0.54 ms, BW 2112 Hz/pixel, 64 phase encoding steps, 16 slices, FOV 220 mm, $3.4 \times 3.4 \times 2$ mm, 3×250 measurements), and stability parameters such as SNR, Signal-to-Fluctuation-Noise Ratio (SFNR), signal drift, fluctuation, and ghosting were calculated according to the recommendations of the FBRIN consortium [45].

For absolute B1 mapping, a pre-saturation turbo-flash B1 mapping sequence was used in two elliptical cylinder phantoms (minor and major axes: 18 and 28 cm), one filled with oil and one filled with tissue-simulating liquid ($\varepsilon_r = 45.3$, $\sigma = 0.87$ S m^{-1}, 56.69% sugar, 37.46% water, 5.85% salt). In the oil phantom the mean flip angle was calculated over a central axial slice for both the integrated and the local body coil; in the tissue-simulating-liquid phantom the flip angle in the center was measured.

The same phantoms were used to measure GRAPPA g-factor maps using a pseudo multiple replica approach [46].

Imaging was performed in a healthy male volunteer (1.87 m, 82 kg). For imaging, a gradient echo sequence was used with a TR of 50 ms and a TE of 4.1 ms with a slice thickness of 10 mm. Axial slices were acquired with a field of view of 350 by 350 mm with an acquisition matrix of 256 by 256 and a bandwidth of 219 Hz/pixel, whereas coronal slices were acquired with a field of view of 500 by 500 mm with an acquisition matrix of 256 by 256 and a bandwidth of 150 Hz/pixel. For each array a static RF shim was calculated to improve homogeneity over the entire field of view. Power limits were calculated using the VOPs from simulation data for each array. These limits were not exceed during the image protocol. The shims were calculated based on axial relative B1 maps using a Nelder-Mead simplex search algorithm that optimized the phases of the input channels at equal amplitudes to minimize three times the standard deviation of the B_1^+ over the entire slice minus the mean of the B_1^+ over the entire slice.

All procedures performed in studies involving human participants were in accordance with the ethical standards of the institutional research committee and with the 1964 Helsinki declaration and its later amendments.

Availability of Data

If the data used for this article is requested through an email to the corresponding author, we will do our best effort to provide it, as far as legal and ethical concerns will allow us to do so.

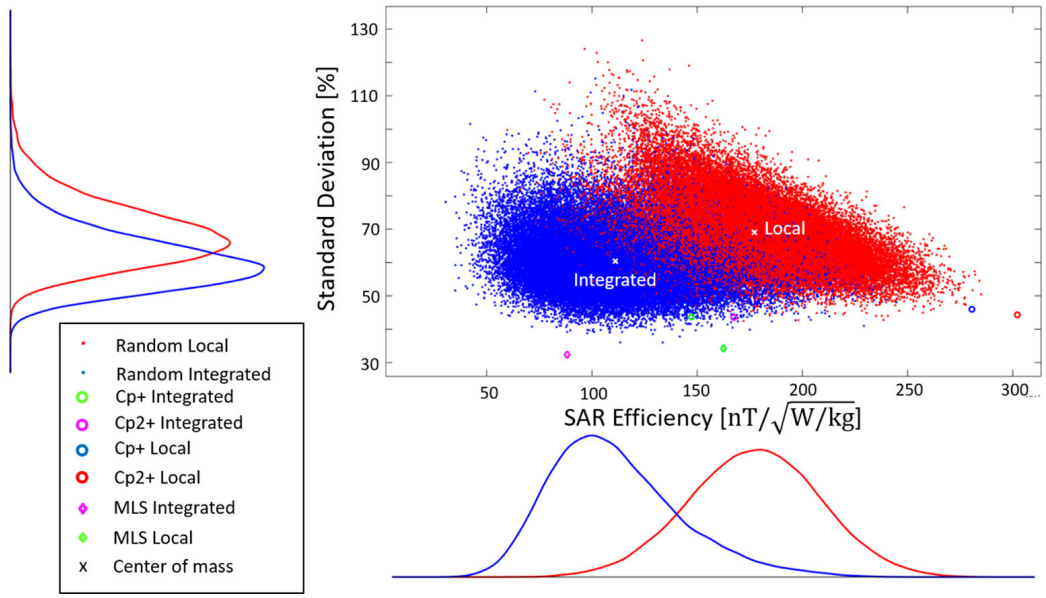

FIGURE 2 | Comparison of homogeneity and SAR efficiency of the local and integrated coils. Standard deviation in [%] of B_1^+ in a central axial slice versus SAR efficiency in [nT$\sqrt{\text{W/kg}}$] for 50,000 random shims and for a MLS shim for both the local array and the integrated array including kernel density plots is shown. The center of mass for each set of shims is indicated with a white cross. While the integrated array shows a slightly better overall performance in terms of standard deviation as a measure of homogeneity, the local array performs better in terms of SAR efficiency. For reference, the first two circular polarized modes (CP modes) for both arrays are shown.

RESULTS

Numerical Simulations

Figure 2 shows the results for 50,000 random shims as well as for an MLS shim for both arrays including kernel density plots. It is apparent that while the integrated array performs slightly better in terms of B_1^+ standard deviation as a measure of homogeneity, the SAR performance of the local array exceeds that of the integrated array considerably. Please note that the different SAR limits for trunk and extremities were not taken into account in this representation. For reference, the first two circularly polarized modes (CP modes) are shown for each array. While the standard deviation is quite similar, the power efficiency differs by approximately a factor of two when comparing both arrays. While elements 3 and 7 of the integrated array are comparably close to the body tissue of the arms, all other elements are much further away and have low power efficiency in the central slice; since in the CP modes all elements transmit with equal power, this leads to an overall low SAR efficiency.

Figure 3 shows the voxel-wise SAR efficiency of the local array (**Figures 3a,b**) and the integrated array (**Figures 3c,d**) as well as the ratio $\text{efficiency}_{\text{integrated}}/\text{efficency}_{\text{local}}$ (**Figures 3e,f**). These figures show that the local array has superior performance in an area of approximately 25 cm along the magnet axis, which is the length of the local coil's elements. In a central axial slice (**Figures 3a,c,e**), the mean ratio is 0.83. Outside of the area directly under the local array, the SAR efficiency of the integrated coil is superior.

Table 1 shows the power budget for both coils when the CP+ mode is applied and the arrays are loaded with the oval phantom filled with tissue-simulating liquid. The values are given relative to the forward power at the feeding network. When the same input power is applied, the local coil delivers approximately three times more power to the sample than the integrated array.

S-Parameter Measurements

The reflection coefficients of the elements of the integrated coil inside the magnet loaded with a healthy male volunteer (1.87 m, 82 kg) were -15.3 ± 7.4 dB (maximum value -5.5 dB). The highest reflection coefficient was observed in the elements close to the arms of the volunteer. Coupling between all elements was below -21.3 dB. The highest coupling occurred between neighboring elements in the upper part of the array, where the distance between the elements and the body was largest.

The reflection coefficients for the local coil were -16.22 ± 4.9 dB (maximum value -13 dB). Coupling between all elements was below -25 dB. The highest coupling occurred between neighboring elements in the dorsal part of the array.

MR Experiments

The integration of the remote body coil had no detectable influence on the QA parameters of the system measured with a local coil. Neither an immediate impact after integration nor a longer-term drift during the following 6 weeks was found; system users did not report any impairments in image

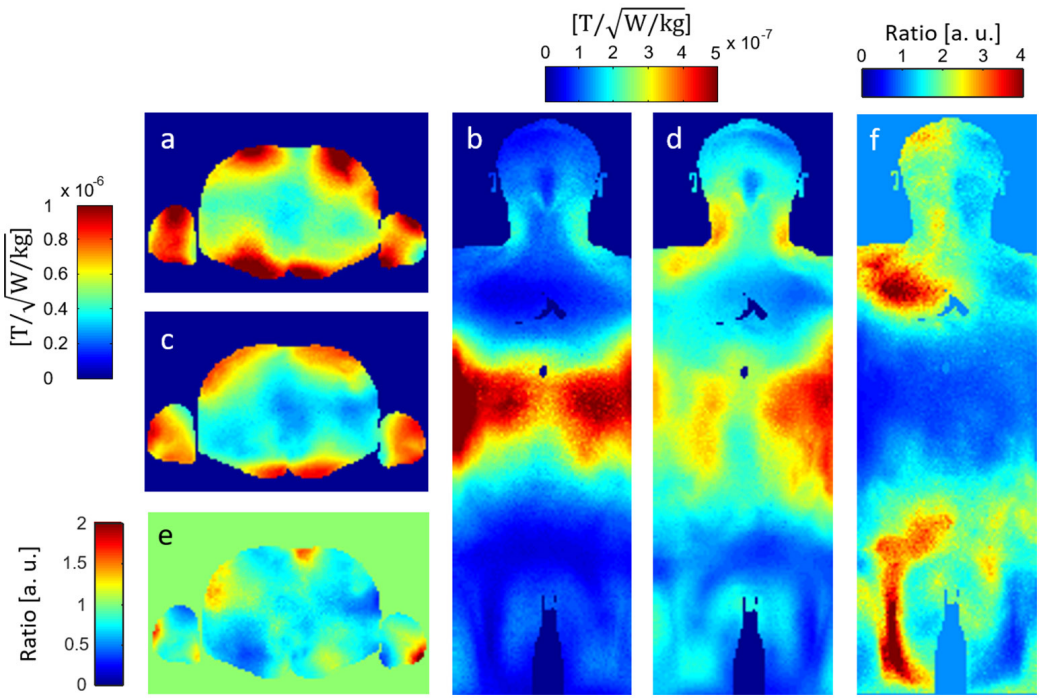

FIGURE 3 | Voxel-wise SAR efficiency of the two coils: **(a,b)** show the voxel-wise SAR efficiency for the local array, whereas **(c,d)** show the voxel-wise SAR efficiency for the integrated array; **(e,f)** show the ratio of the efficiency of the integrated array over the efficiency of the local array. The mean value in **(e)** is 0.83. The local array performs better in a region of approximately 25 cm along the magnet axis. Outside of this region it is outperformed by the integrated array.

TABLE 1 | Power budget obtained by numerical simulation for the CP+ mode for both arrays.

	Integrated array [%]	Local array [%]
Total reflection (includes coupling)	24.8	9.6
Radiated	25.2	14.6
Tuning and Matching networks	11.9	2.1
Coil housing	0	10.4
Bore liner	17.3	0.2
Phantom	20.8	63.3

Each array is loaded with a phantom filled with tissue-simulating liquid. The integrated array has no housing and is directly attached to the bore liner. Tuning and matching networks include the 180° line of the balun. The feeding point is directly at the central feeding network; no further cables or T/R-switches are included.

quality that could be correlated with integration of the remote body coil.

B_1^+ mapping over an axial slice in the oil phantom showed a mean power efficiency of 92 $nT/\sqrt{W}$ for the integrated array and 290 $nT/\sqrt{W}$ for the local array. The power efficiency in the center of the tissue-simulating-liquid phantom was 38 $nT/\sqrt{W}$ for the integrated array and 125 $nT/\sqrt{W}$ for the local array. Power was normalized to the coil plug (end of the high-power RF cables coming from the RFPAs); losses within the coil set-ups themselves (e.g., different cable lengths) degrade the power efficiency. The corresponding B_1^+ maps are shown in **Figures 4a,b**. The region of interest in which B_1^+ was evaluated in the center of the phantom is shown as a black circle. The simulated B_1^+ maps for the same oval phantom in **Figures 4c,d** show good qualitative agreement between simulation and measurement. The power efficiency in the center of the phantom was 50 $nT/\sqrt{W}$ for the integrated array and 150 $nT/\sqrt{W}$ for the local array, corresponding to a difference between simulation and measurement of 31 and 20%.

Figure 5 shows the GRAPPA g-factors for acceleration factors of $R = 2$ and $R = 3$ for the two arrays. The local array shows considerably lower maximum g-factors than the integrated array. The maximum g-factors are 1.73 ($R = 2$) and 3.89 ($R = 3$) for the integrated array and 1.52 ($R = 2$) and 2.54 ($R = 3$) for the local array.

Figure 6 shows gradient echo images of a human volunteer acquired with the integrated body array (**Figures 6a,b**) and the local body array (**Figures 6c,d**) over a large field of view. Again, the coronal view shows a larger effective field of view for the integrated array. The phases of the input channels were 294°, 256°, 107°, 0°, 24°, 23°, 351°, 281° for the flexible array and 10°, 114°, 213°, 143°, 152°, 88°, 311°, 206° for the remote array.

DISCUSSION

This work is targeted toward investigating the feasibility of integrating a multi-channel body array into the space between the bore liner and the gradient coil at 7 T similar to the RF body coils

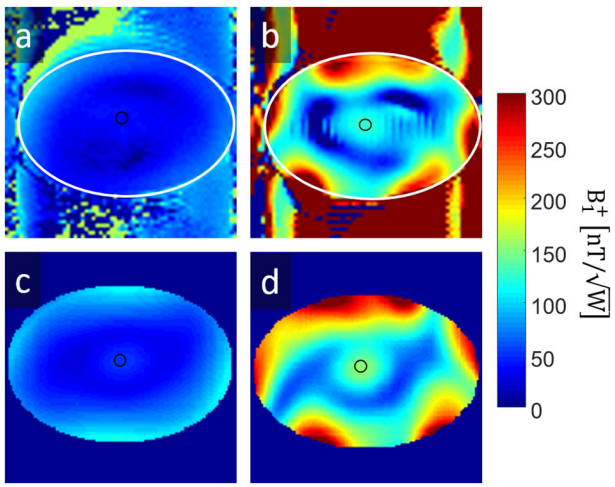

FIGURE 4 | Comparison between measured and simulated data for the two coils. The first row shows B_1^+ maps in the tissue-simulating liquid phantom (white oval) with the ROI in the center marked by the black circle for **(a)** the integrated array and **(b)** the local array, while **(c,d)** show the corresponding results from RF simulations.

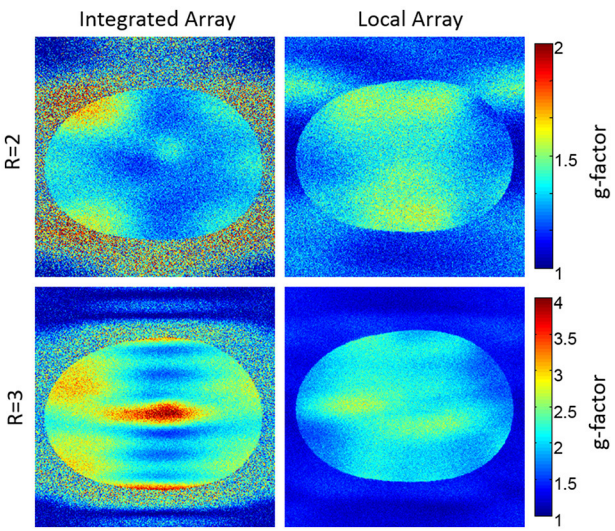

FIGURE 5 | GRAPPA g-factors for the two arrays for acceleration factors of $R = 2$ and $R = 3$. The phantom cross-section is not perfectly elliptical.

used at clinical field strengths. Such an array would free up space within the bore that could be used for dedicated receive arrays and lead to a similar workflow as at lower field strengths.

From the numerical experiments it is apparent that the integrated array slightly improves homogeneity. This improvement comes at a cost in SAR efficiency, at least within the volume encompassed by the local array. Outside the area directly covered by the local array, the SAR efficiency of the integrated array exceeds the efficiency of the local array. The measured g-factors indicate that the receive fields generated by the elements of the integrated coil are not as distinct as in the local coil. Equivalently, the transmit fields do not support as many degrees of freedom, resulting in reduced shimming capability for the integrated array and therefore lower SAR efficiency. Furthermore, it should be noted that these results do not consider different SAR limits for trunk and extremities. The results might change slightly when different limits are taken into account, since the elements of the integrated array that are closest to the body are close to the arms, whereas for the local array the elements are all close to the trunk, and maximum local SAR often occurs at positions close to the meander elements.

The S-parameter measurements show satisfactory decoupling of the integrated array. The fixed tuning is suboptimal, especially for the elements close to the arms where loading can vary heavily depending on patient size and positioning. Since it is not possible to access the coil once it is integrated into the magnet bore, automated matching [47, 48] might be a way to increase the coil's power efficiency.

Quality assurance protocols showed no interaction with a local head coil and no degradation in overall system performance after the integrated array was installed in the system. Whether this is also the case for large unshielded coils placed in the bore was not investigated.

The power efficiency of the integrated array is quite low. For the homogeneous shim it is in the range of the power efficiency of traveling-wave MRI [49]. This is due to the fact that the integrated array's field of view is much larger than that of the local coil. To cope with the lower efficiency, the power for each element has to be increased. Alternatively, a larger number of elements, including elements placed along the longitudinal axis of the magnet, should be beneficial to lower the power per element [50] and, furthermore, increase the degrees of freedom for transmit field control, leading to better capability to achieve excitation field uniformity. Since there is quite a bit of bore liner surface area that can be covered, a higher number of channels could easily be integrated, while the cabling and the necessary electronics can also be placed in the gap between the gradient coil and the bore liner so as not to take up valuable space in the bore.

The increase in g-factors for reception with the integrated array could easily be compensated by using dedicated local receive arrays; these would be straightforward to accommodate due to the increase in available space within the bore. Dedicated receive elements close to the surface of the body would also provide a higher baseline SNR.

The large field of view of such an integrated array might be beneficial for large field of view imaging and for localization. Such an array would also facilitate multi-station examination protocols.

The presented integrated array leaves more space inside the bore, making the bore accessible for larger patients and potentially facilitating the integration of local receive arrays. Also, the large field of view and slightly increased homogeneity could be of benefit. The lower power efficiency of the integrated array indicates the necessity for more powerful amplifiers and/or more elements; this will be the subject of further studies, since the placement of the integrated array allows for the implementation of a large number of elements and their accompanying electronics without reducing bore space. The

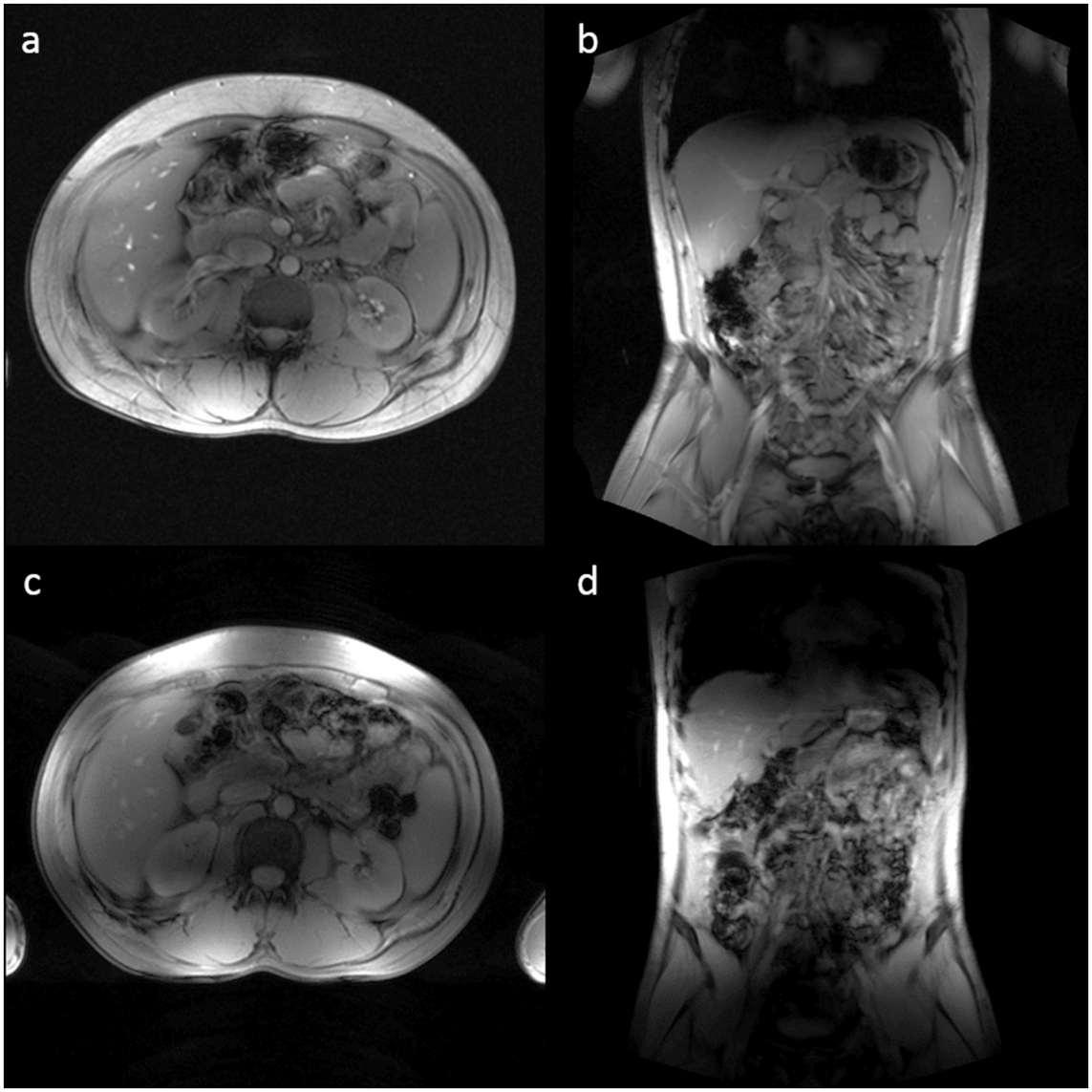

FIGURE 6 | *In vivo* images of a male volunteer acquired with **(a,b)** the integrated body coil and **(c,d)** the local body coil. The axial slices **(a,c)** have a field of view of 350 by 350 cm. The coronal slices **(b,d)** have a field of view of 500 by 500 mm. The images appear subjectively quite homogeneous even though they were acquired only with static RF shims to improve uniformity and no intensity correction was used.

impact of more elements on the SAR efficiency of the array will also be investigated.

ETHICS STATEMENT

This study was carried out in accordance with the recommendations of the ethical standards of the institutional and national research committee with written informed consent from all subjects. All subjects gave written informed consent in accordance with the Declaration of Helsinki. The protocol was approved by the local ethics committee of the University of Duisburg-Essen, Germany.

AUTHOR CONTRIBUTIONS

Project Development: SO, AB, OK, AA, HQ, KS, and ML. Data Collection: SO and AB. Data Analysis: SO, AB, SJ, MG, MV, TF, and ML.

ACKNOWLEDGMENTS

The research leading to these results has received funding from the European Research Council under the European Union's Seventh Framework Programme (FP/2007–2013)/ERC Grant Agreement n. 291903 MRexcite.

REFERENCES

1. Hoult DI, Phil D. Sensitivity and power deposition in a high-field imaging experiment. *J Magn Reson Imaging* (2000) **12**:46–67. doi: 10.1002/1522-2586(200007)12:1<46::AID-JMRI6>3.0.CO;2-D
2. Van de Moortele PF, Akgun C, Adriany G, Moeller S, Ritter J, Collins CM, et al. B(1) destructive interferences and spatial phase patterns at 7 T with a head transceiver array coil. *Magn Reson Med.* (2005) **54**:1503–18. doi: 10.1002/mrm.20708
3. Vaughan JT, Snyder CJ, DelaBarre LJ, Bolan PJ, Tian J, Bolinger L, et al. Whole-body imaging at 7T: preliminary results. *Magn Reson Med*. (2009) **61**:244–8. doi: 10.1002/mrm.21751
4. Umutlu L, Bitz AK, Maderwald S, Orzada S, Kinner S, Kraff O, et al. Contrast-enhanced ultra-high-field liver MRI: a feasibility trial. *Eur J Radiol*. (2013) **82**:760–7. doi: 10.1016/j.ejrad.2011.07.004
5. Wu X, Schmitter S, Auerbach EJ, Ugurbil K, Van de Moortele PF. Mitigating transmit B 1 inhomogeneity in the liver at 7T using multi-spoke parallel transmit RF pulse design. *Quant Imaging Med Surg*. (2014) **4**:4–10. doi: 10.3978/j.issn.2223-4292.2014.02.06
6. Umutlu L, Maderwald S, Kinner S, Kraff O, Bitz AK, Orzada S, et al. First-pass contrast-enhanced renal MRA at 7 Tesla: initial results. *Eur Radiol.* (2013) **23**:1059–66. doi: 10.1007/s00330-012-2666-0
7. Vos EK, Lagemaat MW, Barentsz JO, Futterer JJ, Zamecnik P, Roozen H, et al. Image quality and cancer visibility of T2-weighted magnetic resonance imaging of the prostate at 7 Tesla. *Eur Radiol*. (2014) **24**:1950–8. doi: 10.1007/s00330-014-3234-6
8. Luttje MP, Italiaander MG, Arteaga de Castro CS, van der Kemp WJ, Luijten PR, van Vulpen M, et al. (31) P MR spectroscopic imaging combined with (1) H MR spectroscopic imaging in the human prostate using a double tuned endorectal coil at 7T. *Magn Reson Med.* (2014) **72**:1516–21. doi: 10.1002/mrm.25070
9. Umutlu L, Kraff O, Fischer A, Kinner S, Maderwald S, Nassenstein K, et al. Seven-Tesla MRI of the female pelvis. *Eur Radiol.* (2013) **23**:2364–73. doi: 10.1007/s00330-013-2868-0
10. Theysohn JM, Kraff O, Orzada S, Theysohn N, Classen T, Landgraeber S, et al. Bilateral hip imaging at 7 Tesla using a multi-channel transmit technology: initial results presenting anatomical detail in healthy volunteers and pathological changes in patients with avascular necrosis of the femoral head. *Skeletal Radiol*. (2013) **42**:1555–63. doi: 10.1007/s00256-013-1698-0
11. Chang G, Deniz CM, Honig S, Egol K, Regatte RR, Zhu Y, et al. MRI of the hip at 7T: feasibility of bone microarchitecture, high-resolution cartilage, and clinical imaging. *J Magn Reson Imaging* (2014) **39**:1384–93. doi: 10.1002/jmri.24305
12. von Knobelsdorff-Brenkenhoff F, Tkachenko V, Winter L, Rieger J, Thalhammer C, Hezel F, et al. Assessment of the right ventricle with cardiovascular magnetic resonance at 7 Tesla. *J Cardiovasc Magn Reson.* (2013) **15**:23. doi: 10.1186/1532-429X-15-23
13. Vossen M, Teeuwisse W, Reijnierse M, Collins CM, Smith NB, Webb AG. A radiofrequency coil configuration for imaging the human vertebral column at 7 T. *J Magn Reson*. (2011) **208**:291–7. doi: 10.1016/j.jmr.2010.11.004
14. van der Velden TA, Italiaander M, van der Kemp WJ, Raaijmakers AJ, Schmitz AM, Luijten PR, et al. Radiofrequency configuration to facilitate bilateral breast P MR spectroscopic imaging and high-resolution MRI at 7 Tesla. *Magn Reson Med.* (2015) **74**:1803–10. doi: 10.1002/mrm.25573
15. Brown R, Storey P, Geppert C, McGorty K, Klautau Leite AP, Babb J, et al. Breast MRI at 7 Tesla with a bilateral coil and robust fat suppression. *J Magn Reson Imaging* (2014) **39**:540–9. doi: 10.1002/jmri.24205
16. Fischer A, Maderwald S, Johst S, Orzada S, Ladd ME, Umutlu L, et al. Initial evaluation of non-contrast-enhanced magnetic resonance angiography in patients with peripheral arterial occlusive disease at 7 T. *Invest Radiol*. (2014) **49**:331–8. doi: 10.1097/RLI.0000000000000044
17. Collins CM, Liu W, Swift BJ, Smith MB. Combination of optimized transmit arrays and some receive array reconstruction methods can yield homogeneous images at very high frequencies. *Magn Reson Med.* (2005) **54**:1327–32. doi: 10.1002/mrm.20729
18. Metzger GJ, Snyder C, Akgun C, Vaughan T, Ugurbil K, Van de Moortele PF. Local B1+ shimming for prostate imaging with transceiver arrays at 7T based on subject-dependent transmit phase measurements. *Magn Reson Med.* (2008) **59**:396–409. doi: 10.1002/mrm.21476
19. Saekho S, Yip CY, Noll DC, Boada FE, Stenger VA. Fast-kz three-dimensional tailored radiofrequency pulse for reduced B1 inhomogeneity. *Magn Reson Med.* (2006) **55**:719–24. doi: 10.1002/mrm.20840
20. Grissom W, Yip CY, Zhang Z, Stenger VA, Fessler JA, Noll DC. Spatial domain method for the design of RF pulses in multicoil parallel excitation. *Magn Reson Med.* (2006) **56**:620–9. doi: 10.1002/mrm.20978
21. Katscher U, Bornert P, Leussler C, van den Brink JS. Transmit SENSE. *Magn Reson Med.* (2003) **49**:144–50. doi: 10.1002/mrm.10353
22. Orzada S, Maderwald S, Poser BA, Bitz AK, Quick HH, Ladd ME. RF excitation using time interleaved acquisition of modes (TIAMO) to address B1 inhomogeneity in high-field MRI. *Magn Reson Med*. (2010) **64**:327–33. doi: 10.1002/mrm.22527
23. Adriany G, Van de Moortele PF, Wiesinger F, Moeller S, Strupp JP, Andersen P, et al. Transmit and receive transmission line arrays for 7 Tesla parallel imaging. *Mag Reson Med*. (2005) **53**:434–45. doi: 10.1002/mrm.20321
24. Metzger GJ, van de Moortele PF, Akgun C, Snyder CJ, Moeller S, Strupp J, et al. Performance of external and internal coil configurations for prostate investigations at 7 T. *Magn Reson Med*. (2010) **64**:1625–39. doi: 10.1002/mrm.22552
25. Snyder CJ, Delabarre L, Moeller S, Tian J, Akgun C, Van de Moortele PF, et al. Comparison between eight- and sixteen-channel TEM transceive arrays for body imaging at 7 T. *Magn Reson Med*. (2012) **67**:954–64. doi: 10.1002/mrm.23070
26. Orzada S, Quick HH, Ladd ME, Bahr A, Bolz T, Yazdanbakhsh P, et al. A flexible 8-channel transmit/receive body coil for 7 T human imaging. In: *Proceedings of the 17th Scientific Meeting, International Society for Magnetic Resonance in Medicine*, Honolulu (2009). p. 2999.
27. Winter L, Kellman P, Renz W, Grassl A, Hezel F, Thalhammer C, et al. Comparison of three multichannel transmit/receive radiofrequency coil configurations for anatomic and functional cardiac MRI at 7.0T: implications for clinical imaging. *Eur Radiol*. (2012) **22**:2211–20. doi: 10.1007/s00330-012-2487-1
28. Graess A, Renz W, Hezel F, Dieringer MA, Winter L, Oezerdem C, et al. Modular 32-channel transceiver coil array for cardiac MRI at 7.0T. *Magn Reson Med.* (2014) **72**:276–90. doi: 10.1002/mrm.24903
29. Versluis MJ, Tsekos N, Smith NB, Webb AG. Simple RF design for human functional and morphological cardiac imaging at 7tesla. *J Magn Reson*. (2009) **200**:161–6. doi: 10.1016/j.jmr.2009.06.014
30. Raaijmakers AJ, Ipek O, Klomp DW, Possanzini C, Harvey PR, Lagendijk JJ, et al. Design of a radiative surface coil array element at 7 T: the single-side adapted dipole antenna. *Magn Reson Med*. (2011) **66**:1488–97. doi: 10.1002/mrm.22886
31. Oezerdem C, Winter L, Graessl A, Paul K, Els A, Weinberger O, et al. 16-channel bow tie antenna transceiver array for cardiac MR at 7.0 tesla. *Magn Reson Med.* (2016) **75**:2553–65. doi: 10.1002/mrm.25840
32. Raaijmakers AJ, Italiaander M, Voogt IJ, Luijten PR, Hoogduin JM, Klomp DW, et al. The fractionated dipole antenna: a new antenna for body imaging at 7 Tesla. *Magn Reson Med.* (2016) **75**:1366–74. doi: 10.1002/mrm.25596
33. Winter L, Ozerdem C, Hoffmann W, Santoro D, Muller A, Waiczies H, et al. Design and evaluation of a hybrid radiofrequency applicator for magnetic resonance imaging and RF induced hyperthermia: electromagnetic field simulations up to 14.0 Tesla and proof-of-concept at 7.0 Tesla. *PLoS ONE* (2013) **8**:e61661. doi: 10.1371/journal.pone.0061661
34. Willinek WA, Gieseke J, Kukuk GM, Nelles M, Konig R, Morakkabati-Spitz N, et al. Dual-source parallel radiofrequency excitation body MR imaging compared with standard MR imaging at 3.0 T: initial clinical experience. *Radiology* (2010) **256**:966–75. doi: 10.1148/radiol.10092127
35. Vernickel P, Roschmann P, Findeklee C, Ludeke KM, Leussler C, Overweg J, et al. Eight-channel transmit/receive body MRI coil at 3T. *Magn Reson Med.* (2007) **58**:381–9. doi: 10.1002/mrm.21294
36. Vaughan JT, Adriany G, Snyder CJ, Tian J, Thiel T, Bolinger L, et al. Efficient high-frequency body coil for high-field MRI. *Magn Reson Med*. (2004) **52**:851–9. doi: 10.1002/mrm.20177
37. Vaughan JT, Snyder C, Delabarre L, Tian J, Adriany G, Andersen P, et al. Clinical imaging at 7T with a 16 channel whole body coil and 32 receive

channels. In: *Proceedings of the 17th Scientific Meeting, International Society for Magnetic Resonance in Medicine*, Honolulu (2009). p. 392.
38. Deniz CM, Vaidya MV, Sodickson DK, Lattanzi R. Radiofrequency energy deposition and radio frequency power requirements in parallel transmission with increasing distance from the coil to the sample. *Magn Reson Med.* (2016) **75**:423–32. doi: 10.1002/mrm.25646
39. Bitz AK, Brote I, Orzada S, Kraff O, Maderwald S, Quick HH, et al. An 8-channel add-on RF shimming system for whole-body 7 Tesla MRI including real-time SAR monitoring. In: *Proceedings of the 17th Scientific Meeting, International Society for Magnetic Resonance in Medicine*, Honolulu (2009). p. 4767.
40. Rietsch SHG, Quick HH, Orzada S. Impact of different meander sizes on the RF transmit performance and coupling of microstrip line elements at 7 T. *Med Phys.* (2015) **42**:4542–52. doi: 10.1118/1.4923177
41. Watkins RD, Caverly RH, Doherty WE. 298MHz micro miniature 2KW transmit receive switch for 7.0 Tesla TR Arrays. *Proc Intl Soc Mag Reson Med.* (2012) **20**:2686.
42. Christ A, Kainz W, Hahn EG, Honegger K, Zefferer M, Neufeld E, et al. The Virtual Family–development of surface-based anatomical models of two adults and two children for dosimetric simulations. *Phys Med Biol.* (2010) **55**:N23–38. doi: 10.1088/0031–9155/55/2/N01
43. Eichfelder G, Gebhardt M. Local specific absorption rate control for parallel transmission by virtual observation points. *Magn Reson Med.* (2011) **66**:1468–76. doi: 10.1002/mrm.22927
44. Nelder JA, Mead R. A simplex-method for function minimization. *Comput J.* (1965) **7**:308–13. doi: 10.1093/comjnl/7.4.308
45. Friedman L, Glover GH. Report on a multicenter fMRI quality assurance protocol. *J Magn Reson Imaging* (2006) **23**:827–39. doi: 10.1002/jmri.20583
46. Robson PM, Grant AK, Madhuranthakam AJ, Lattanzi R, Sodickson DK, McKenzie CA. Comprehensive quantification of signal-to-noise ratio and g-factor for image-based and k-space-based parallel imaging reconstructions. *Magn Reson Med.* (2008) **60**:895–907. doi: 10.1002/mrm.21728
47. Keith GA, Rodgers CT, Hess AT, Snyder CJ, Vaughan JT, Robson MD. Automated tuning of an eight-channel cardiac transceive array at 7 Tesla using piezoelectric actuators. *Magn Reson Med.* (2015) **73**:2390–7. doi: 10.1002/mrm.25356
48. Venook RD, Hargreaves BA, Gold GE, Conolly SM, Scott GC. Automatic tuning of flexible interventional RF receiver coils. *Magn Reson Med.* (2005) **54**:983–93. doi: 10.1002/mrm.20616
49. Brunner DO, Paska J, Froehlich J, Pruessmann KP. Traveling-wave RF shimming and parallel MRI. *Magn Reson Med.* (2011) **66**:290–300. doi: 10.1002/mrm.22817
50. Guerin B, Gebhardt M, Serano P, Adalsteinsson E, Hamm M, Pfeuffer J, et al. Comparison of simulated parallel transmit body arrays at 3 T using excitation uniformity, global SAR, local SAR, and power efficiency metrics. *Magn Reson Med*. (2015) **73**:1137–50. doi: 10.1002/mrm.25243

Conflict of Interest Statement: The authors declare that the research was conducted in the absence of any commercial or financial relationships that could be construed as a potential conflict of interest.